Ocean Engineering 263 (2022) 112383

Contents lists available at ScienceDirect

Ocean Engineering

journal homepage: www.elsevier.com/locate/oceaneng

# Effect of oil properties on spilled oil recovery using a mechanism coupling surface vortices and cyclone separation

Meng Yang [a,b], Lin-tong Hou [a,b], Li-song Wang [a,b], Shuo Liu [a,*], Jing-yu Xu [a,b,**]

[a] Institute of Mechanics, Chinese Academy of Sciences, Beijing, 100190, China
[b] School of Engineering Sciences, University of Chinese Academy of Sciences, Beijing, 100049, China

ARTICLE INFO

*Keywords:*
Oil spill
Free-surface vortex
Cyclone separation
Crude oil
Recovery efficiency

ABSTRACT

Oil spills can cause severe harm and environmental pollution. Among the various treatment methods available, those that utilize hydrodynamic properties are more environmentally friendly and efficient. In this study, a free-surface vortex method was used to recover crude oil, and the flow process of crude oil with a high viscosity and density in a vortex was studied by conducting scale–scale laboratory experiments. The motion of the oil phase in the same-scale flow field was simulated using a commercial simulation software (ANSYS Fluent), and the tangential velocity distribution in the cylindrical coordinate system was used to reflect the motion of the oil phase. The experimental and simulation results demonstrate that a vortex can be used for oil recovery. The flow and recovery efficiency of crude oil were simulated and compared with the flow properties of a white oil with a low viscosity and density. Crude oil existed more in the form of large droplets in the flow, and the oil core was denser after forming a vortex. The experimental results revealed that the flow performance of crude oil was worse than that of white oil. The recovery efficiency of crude oil after passing through the vortex was lower than that of white oil. In addition, the recovery system was connected to a cyclone separation device. The feasibility of cyclone separation in offshore oil–water separation was verified by comparing the separation efficiency of the crude and white oils. The separation efficiency of crude oil was related to the split ratio. Within a certain range, the separation efficiency increases linearly with the split ratio. Combined with the principle model and numerical simulation results, the vortex motion was described in a three-dimensional space. The generalization of the application range of the recovery and separation method was summarized.

## 1. Introduction

Oil pollution is a severe environmental problem in oceans (Liu and Wirtz, 2009; Eronat et al., 2019). The increasing demand for energy has increased the probability of marine oil spill accidents. Oil spills with a discharge volume of more than 100,000 gallons are considered major oil spills (Ventikos et al., 2004; Abhinav and Pradipta, 2021); these include the oil spills of offshore drilling platforms in the Gulf of Mexico and 19-3 in Penglai Bay (Alves et al., 2014, 2015). Serious oil spill accidents not only cause environmental pollution but also lead to casualties, causing pollution in large areas of the sea and incalculable economic losses (Wei et al., 2015; Cao et al., 2021; Yu et al., 2020).

Oil spill recovery methods can be divided into physical, chemical, and biological methods (Etkin and Nedwed, 2021; Bayat et al., 2015; Kandanelli et al., 2018). Chemical and biological methods have obvious disadvantages, such as the high cost involved and the poor applicability of biological methods. Physical methods have been widely used owing to their low cost and easy applicability, but they have insufficient recovery capacities, while chemical and biological methods have high efficiencies (Giron-Sierra et al., 2015; Zhang et al., 2016; Etkin and Nedwed, 2021). A common physical method of recovering oil spills is using machinery such as oil skimmers. Several types of oil skimmers, such as vacuum oil and weir skimmers, have been developed (Ornitz and Champ, 2002; Fingas, 2011). These skimmers operate based on their shapes or the pressure within a space (Tkalich, 2000; Ventikos et al., 2004). In this study, a novel oil skimmer is developed. It is surrounded by steel plates and has a simple structure. A cylindrical flow field can be formed inside it. A free-surface vortex can be formed inside the skimmer, relying on the flow properties of the vortex to handle large volume flow rate of liquid with in a shorter time and obtained larger oil content as the liquid

* Corresponding author.
** Corresponding author. Institute of Mechanics, Chinese Academy of Sciences, Beijing, 100190, China.
*E-mail addresses:* liushuo@imech.ac.cn (S. Liu), xujingyu@imech.ac.cn (J.-y. Xu).

https://doi.org/10.1016/j.oceaneng.2022.112383
Received 30 January 2022; Received in revised form 12 August 2022; Accepted 21 August 2022
Available online 27 September 2022

mixture has been enriched by the hydrocyclone (An et al., 2021). Experimental tests indicate that the vortex skimmer has a higher processing capacity than other skimmers.

The velocity distribution of the vortex reflects the movement trend of liquids in a space. Various researchers have studied vortex motion in a two-dimensional (2D) plane (Rankine, 1858; Rosenhead, 1930; Burgers, 1948; Einstein and Li, 1955; Vatistas et al., 1988; Mih, 1990). Their research focused on the tangential velocity distribution of the vortex, with several velocity models describing the movements of the vortex being proposed. These models can represent the trend of the velocity changes very well. However, a three-dimensional (3D) description of the vortex is required to study the characteristics of the newly developed skimmer. Some researchers have observed that a free-surface vortex can drag objects from the free surface to the bottom of the vortex. Khazam and Krestra (2008) studied the sedimentation of suspended solids in liquids in industrial agitation tanks. Their study revealed the primary mechanism to be solid settlement and demonstrated that a stable vortex is an effective method for achieving solid settlement. Xu et al. (2020) studied the effects of surface vortices on the sedimentation and dispersion of suspended particles in a stirred tank. Through experiments and numerical simulations, they analyzed the sedimentation process, distribution, and power consumption of the particles. They observed that the average dispersion index was related to the degree of sedimentation of the suspended particles. The structure of the vortex had a greater impact on the sedimentation of suspended particles on the surface. However, fewer studies have been conducted on the drag effect of the vortex on the fluid at the free surface, making it necessary to investigate the motion law of oil in a vortex. Some researchers have studied the space velocity circulation of vortex model and further explored these models from the perspective of velocity circulation changes (Mulligan et al., 2016, 2019; Chan et al., 2022). Studies have focused on the vertical velocity components at the outlet and investigated the relationship between the height of the model and vortex dimensions. Some semi-empirical conclusions have been obtained by performing certain experiments (Shemshi and Kabiri-Samani, 2016; Kumar et al., 2017; Tastan and Yildirim, 2018).

Although free-surface vortex skimmers recover oil spills on the sea surface, the recovered liquid has a high water content. If the recovered liquid is not treated, the efficiency of oil spill recovery decreases significantly. Cyclone separation devices are common devices used for oil–water separation under the premise of occupying a small space. For a mixed liquid with a high water content, it is advisable to use a guide vane to separate the liquid. Guide vanes can be divided into spiral, inclined flat, and arc vanes. Fig. 1 (a) shows the guide vanes used in some studies (Shi et al., 2012; Wang et al., 2019; Kataoka et al., 2008, 2009; Matsubayashi et al., 2012; Liu et al., 2020; Liu and Bai, 2016). In this study, a 3D printed polymer material diversion structure formed by sweeping was used, as shown in Fig. 1 (b). The flow direction changed under the influence of the guide vane, and the axial flow became a strongly swirling flow. Further, the water and oil were separated by centrifugal force. Axial cyclones have better separation effects (Tsai et al., 2004; Hsiao et al., 2010; Liow and Oakman, 2018); therefore, this study combined an oil skimmer with an axial cyclone to develop a novel oil spill recovery and separation device. Research on the oil collected from the free surface using an oil skimmer and separated by an axial cyclone is necessary for the further application of this oil spill recovery and separation technology.

The motion of a vortex to recover oil spills has been partially investigated in previous studies (Yang et al., 2020; An et al., 2021). To further study the motion of a vortex, a 3D control equation and 2D distribution model of vortex velocity were combined to derive the vortex velocity in a 3D space. We begin with the tangential velocity and expand the use of the tangential velocity model. To investigate the applicability of the recovery and separation technique, the recovery and separation processes of different oils were compared in this study. This paper presents a systematic experimental test and Computational Fluid Dynamics

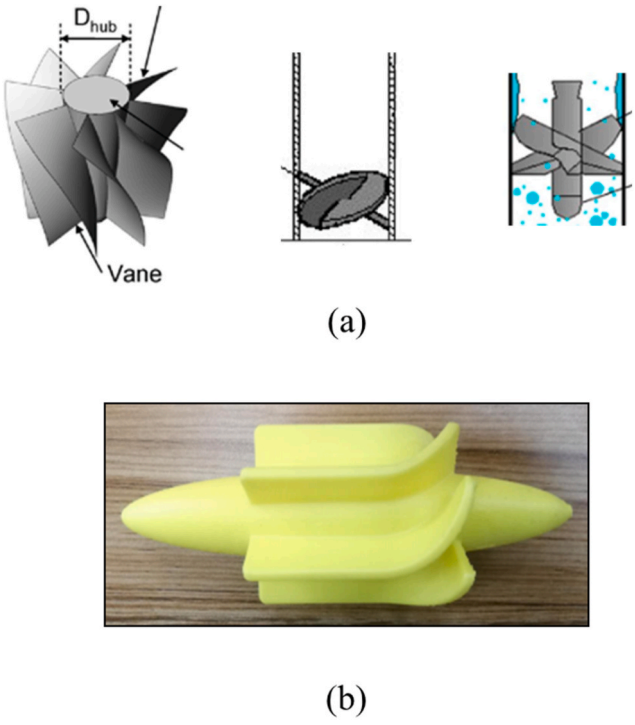


**Fig. 1.** Guide vanes, (a) guide vanes in past studies, (b) guide vanes in this study.

(CFD) analysis. The phenomenon observed in the experiment using the oil skimmer was compared with the simulation results, and the velocity distribution law was analyzed from the simulation results. An analysis of the experimental results further revealed the mechanisms behind the oil spill recovery and separation technology when used at sea. The experimental tests and simulations used crude oil with a high density and viscosity and white oil with a low density and viscosity. The effects of the oil properties on the effectiveness of the recovery and separation technology were studied.

## 2. Materials and methods

### 2.1. Experimental facilities

Vortex recovery and cyclone separation experiments were performed in this study. A schematic of the experimental equipment and connection is shown in Fig. 2 (a). The flow field size of the test pool was 4.04 m × 2.01 m × 0.75 m (length × width × depth). The experimental device consisted of two parts, an oil skimmer and a cyclone separator, and their design details are shown in Fig. 2 (b) and Fig. 2 (c), respectively. Both the height and diameter of the skimmer were 300 mm. The vortex oil skimmer that was submerged in water included a cylindrical metal container with an outlet pipe connected to the bottom. The skimmer used buoys that allowed it to float in the water. The bottom of the skimmer was piped into an electric submersible pump to power the recovery operation. The suction power of the electric submersible pump was adjusted using a frequency converter, and the flow was controlled. The frequency varied from 20 to 40 Hz, with an incremental increase of 5 Hz each time. The entrance flow rate was sensitive to pump frequency and valve opening degree. The cyclone separator was a hydrocyclone with an axial inlet. The hydrocyclone had two underflow ports in the radial direction that water flowed out of. It also had an overflow port in the axial direction through which oil flowed to the center. A guide vane was arranged at the front end of the cyclone, and the second half of the pipe was tapered. The axial length of the cyclone separator was approximately 1 m. The diameter of the inlet was 32 mm, and the

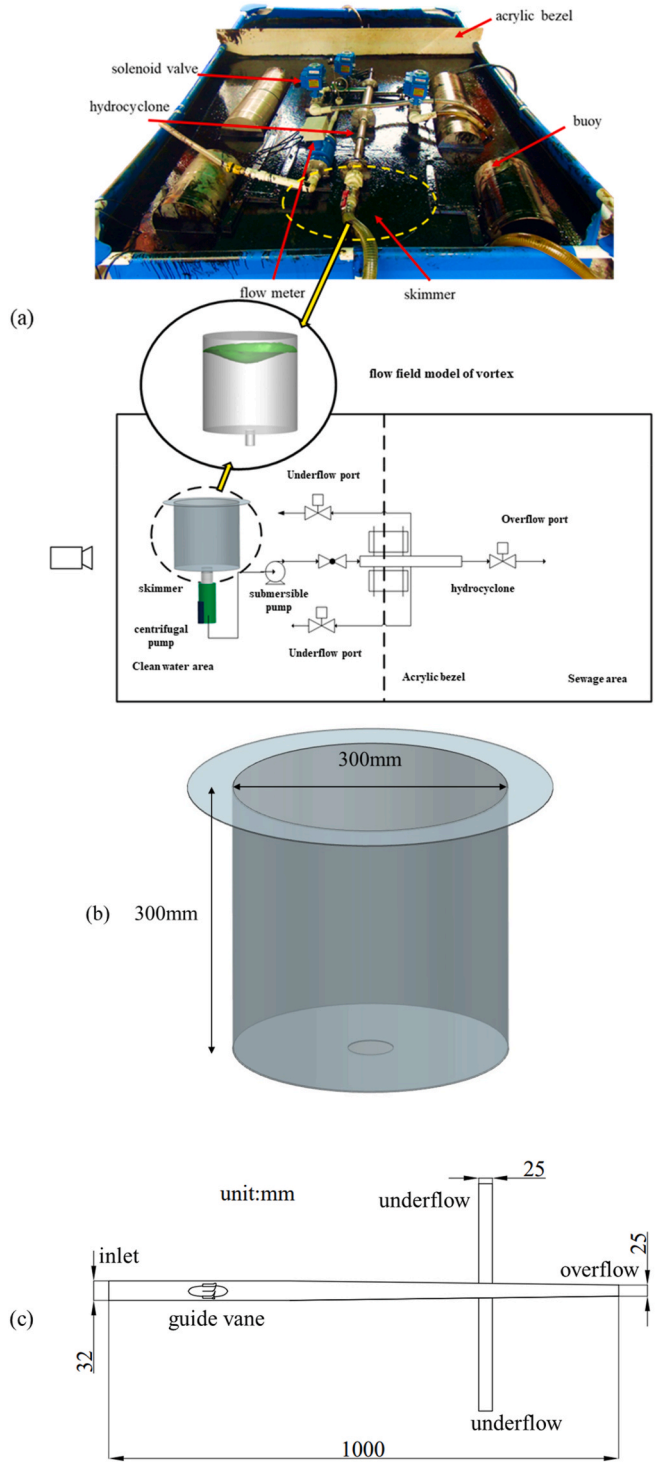


**Fig. 2.** (a) Schematic of the experimental equipment and its connection, (b) designs of the skimmer, (c) designs of the hydrocylcone.

diameter of each outlet was 25 mm. Solenoid valves were installed at the overflow and underflow ports, and their opening degree was controlled by a programmable logic controller program, the adjustment accuracy of which was 1%.

The liquid used in the experiment was composed of two parts. The highest content was tap water, which filled the test pool. The tested oil spill on the water surface was crude oil from the Bohai Sea; its properties are discussed in Section 2.2. The tested white oil was a type of light yellow lubricating oil that was lighter and less viscous than crude oil. Crude oil was dumped into to the test pool to simulate a real sea surface oil spill.

The underflow pipe of the experimental equipment simulated a sea discharge pipe of an offshore treatment device, where the treated seawater would eventually return to the marine environment. The overflow pipe simulated a pipeline connecting the offshore treatment device to an offshore platform or ship. The discharge was a high-oil-content separated liquid. To maintain the continuity of the experiment and reflect the separation effect, the underflow and overflow ports were separated by an acrylic plate so that the test pool was divided into clean water and sewage areas.

The flow rate of the experiment ranged from 8 to approximately 40 L/min. The flow process is summarized as follows. Under the action of a centrifugal pump and electric submersible pump, a vortex was generated in the oil skimmer, and the floating oil on the surface flowed through the pump with the water mixture and then flowed through the guide vane inside the cyclone separation device. Under the action of the vane, oil and water were separated from each other. The oil phase flowed to the overflow outlet along the axis of the separation device and was discharged into the sewage area. The water phase was discharged into the clean water area along the tangential underflow pipe.

The state of the small amount of crude oil on the water surface is shown in Fig. 3, and the amount of oil gradually increased from left to right. A small amount of crude oil could not cover the water surface evenly. There was a continuous area and large, scattered oil droplets. After the oil volume increased slightly, the crude oil still could not fully occupy the gas–liquid interface, with a large number of holes on the oil film. Owing its high surface tension, crude oil cannot be laid flat on a water surface as small particles under the action of gravity; however, this state can be achieved when the oil is aggregated. The oil film could not fully occupy the interface until the average thickness of the oil film exceeded approximately 2 mm.

### 2.2. Measurement and comparison of oil properties

In the experiment, the temperature was often below 25 °C and the viscosity of crude oil was larger than 10 Pa s under such condition. To extend the method in this study to variant oil viscosities, reducing the viscosity of crude oil is necessary in the tests. Hence, considering environment temperature, wider range of viscosity was obtained by blending crude and white oil with different ratios as presented in Fig. 7.

To identify the density and viscosity–temperature characteristics of the crude oil and oil blended with diesel oil, rheological tests were performed on the oil samples. A Hakke RS6000 advanced rotating rheometer (Thermo Fisher Scientific) was used to conduct the rheology experiment. Measuring rotors Z38 and Z43 were used in the experiment. Water bath heating was adopted to keep the temperature of the oil sample constant in the experiment.

The densities of crude oil at 20–70 °C were measured, and the measurement results were fitted to an exponential function curve, as shown in Fig. 4. As the temperature increased, the density of the crude oil gradually decreased from approximately 966 kg/m$^3$ to approximately 930 kg/m$^3$. The logarithmic coordinate was used for temperature; therefore, it can be approximated that the relationship between the temperature and density of crude oil is logarithmic. The temperature of the test pool was measured during the experiment. The field temperature was approximately 15 °C and the crude oil density was approximately 975 kg/m$^3$. When measuring the temperature, there were measurement errors; therefore, the error bars are plotted in Fig. 4. Because the temperature errors were all less than 0.2 °C, the error bars were magnified 50 times. The fluctuation amplitude can be kept almost the same, and the errors have little effect on the density-fitting result.

The crude oil sample was placed in a rotating cylinder cup Z43 and installed in the rheometer. The temperature of the oil sample was maintained during the measurement using a bath water temperature control system. For the same oil sample, the temperature was measured

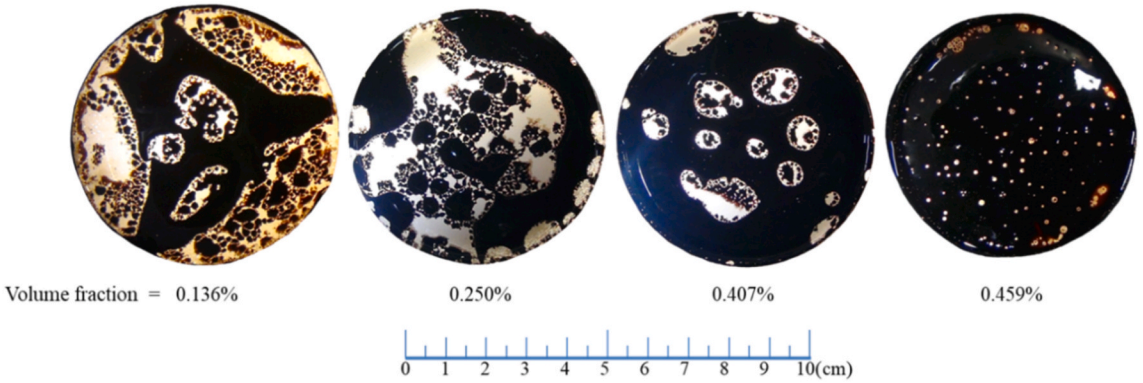


**Fig. 3.** State in which a small amount of crude oil floats on the surface of water.

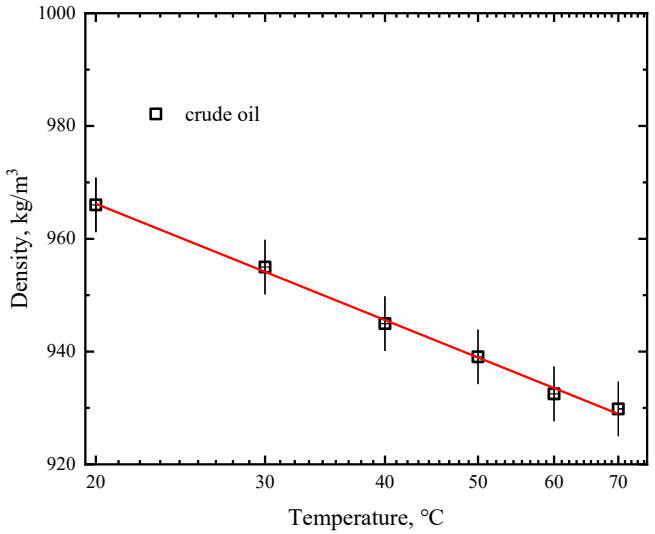


**Fig. 4.** Fitting curve of crude oil density at different temperatures.

from low to high, and the temperature was changed from 5 to 50 °C. To compare the rheological properties of the oil sample to those of white oil, the same test was performed on white oil at 15 °C. The viscosity of white oil is approximately 0.03 Pa s, which is much smaller than that of crude oil. Different volume fractions of diesel oil were added to the crude oil samples.

Fig. 5 (a) shows the shear stress-shear rate curves of crude oil and white oil at different temperatures. The data demonstrates that the relationship between the shear stress and shear rate of crude oil at different temperatures is linear. As the shear rate increases, the shear stress gradually increases. As the temperature increases, the rate of change of the shear stress of crude oil decreases rapidly, and the slope of the curve decreases rapidly. The slope of the white oil curve is much smaller than that of the crude oil curve. Fig. 5 (b) shows the viscosity–shear rate curves of crude oil and white oil at different temperatures. Even if the temperature rises to 50 °C, the viscosity of crude oil is still considerably higher than that of white oil. To obtain different viscosities, the viscosity can be adjusted by changing the temperature; however, the adjustment range is limited. For laboratory experiments, adding diluents can be used to acquire more viscosity data. In this experiment, diesel was used as the diluent. Different amounts of diesel oil were added to the crude oil, and oil products with different properties were obtained.

Fig. 6 shows the shear stress–shear rate curves of crude oil samples with different volume fractions of diesel oil. The shear stress of the sample after adding diesel oil is significantly reduced, and the viscosity of the sample containing 25% diesel can behave like crude oil heated to 50 °C. The rheological properties of the samples with different volume fractions of diesel at various temperatures were tested. As shown in Fig. 7, the viscosity–temperature curves of each sample were obtained. As the proportion of diesel increases, the viscosity of the oil sample gradually decreases. When more than 15% of diesel is added, the density of crude oil is reduced to less than 20% of the original. During the experiment, the viscosity reduction of crude oil samples was mainly

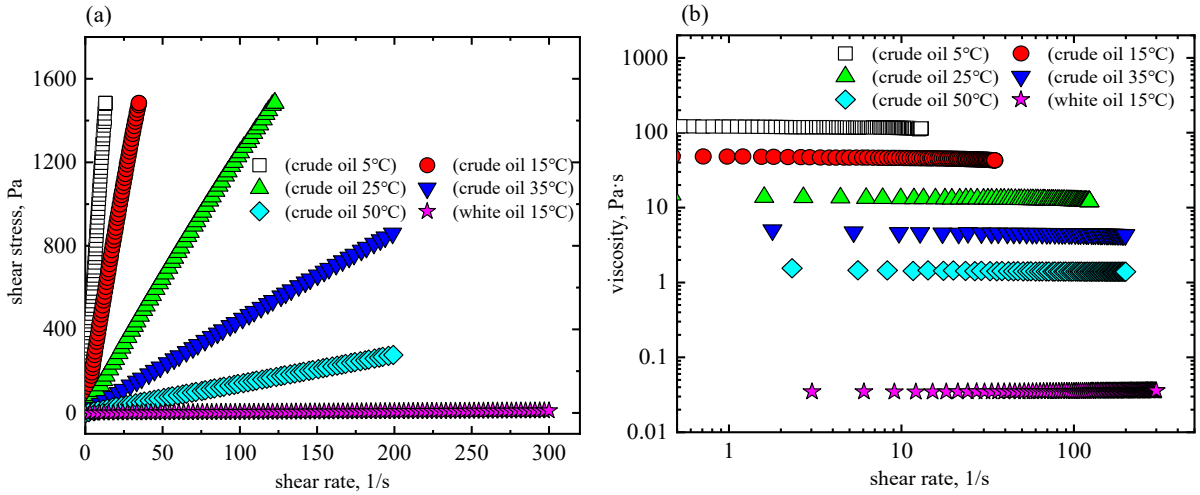


**Fig. 5.** (a) Shear stress and (b) viscosity of oil samples.

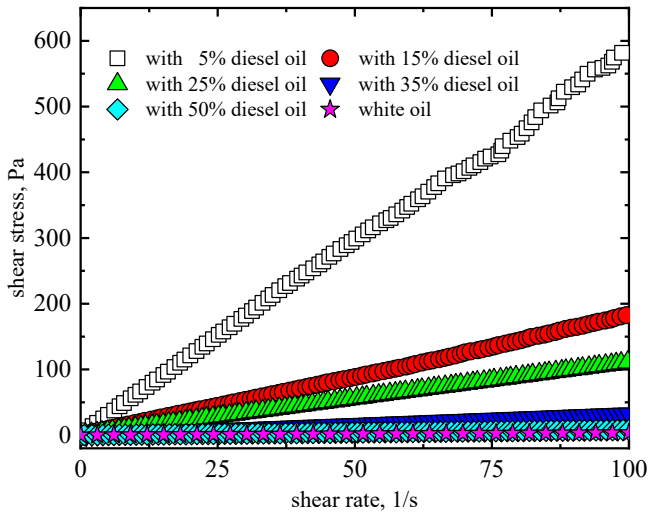


**Fig. 6.** Shear stress of oil samples with diesel oil.

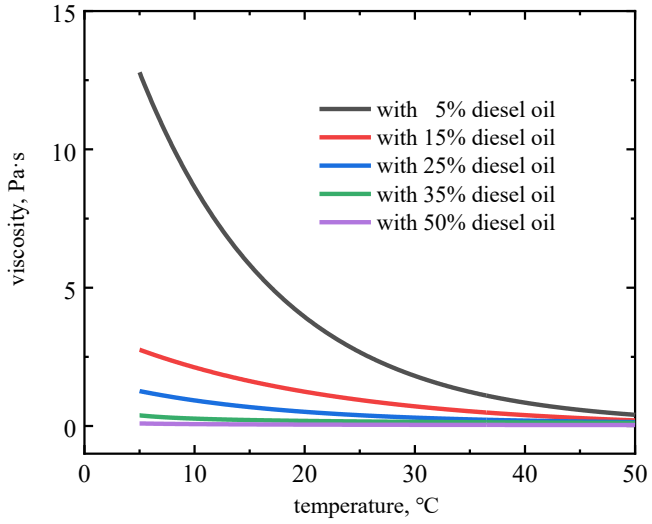


**Fig. 7.** Viscosity of oil samples with diesel oil.

accomplished by adding diesel oil. Heat is used as a supplement to prevent the excessive adhesion of crude oil to the experimental facilities.

## 3. Model and numerical method

### 3.1. Flow models

The free-surface vortex is described by a governing equation, and its continuity and momentum conservation equations can be constructed. The classic vortex structure is illustrated in Fig. 8. The ideal vortex motion is a steady axisymmetric structure that rotates around a fixed axis at the symmetry line of the section. Therefore, to facilitate the description of the motion state of the vortex, the motion in the three directions of $x$, $y$, and $z$ in the Cartesian coordinate system was transformed into tangential, radial, and axial motions in the cylindrical coordinate system, respectively, which are reflected by the subscripts $\theta$, $r$, and $z$ respectively.

The free-surface vortex is an incompressible flow; thus, its density is constant. The continuity equation takes the following form:

$$\frac{\partial V_{qr}}{\partial r}+\frac{\partial V_{qz}}{\partial z}+\frac{V_{qr}}{r}=0 \tag{1}$$

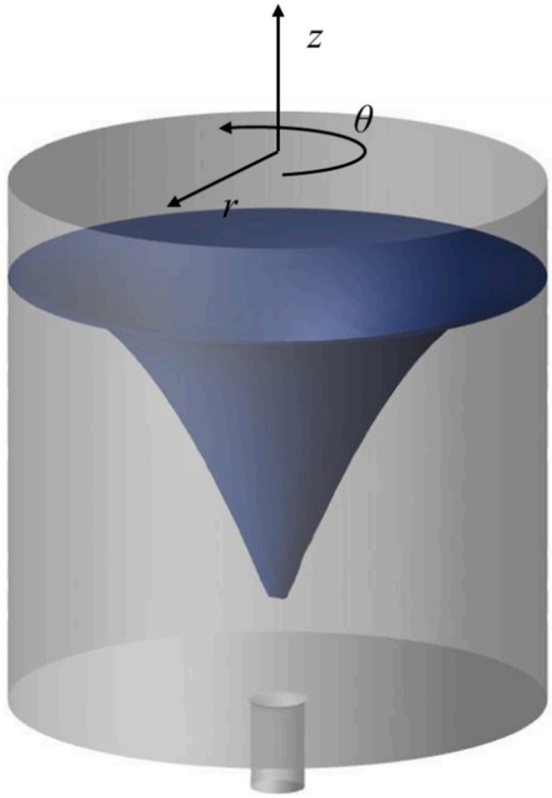


**Fig. 8.** Schematic of typical vortex structure.

where $V$ is the velocity. The first subscript indicates the $q$th phase, and the second subscript indicates the speed direction.

The ideal vortex motion is steady and unrelated to time. However, the formation process of the vortex was investigated in this study, and thus the time-derivative terms of the motion in each direction were temporarily retained. Because of the axis symmetry, all $\partial/\partial\theta$ terms in the equation are equal to zero. Finally, the following momentum conservation equation was obtained:

$$\frac{\partial V_{q\theta}}{\partial t}+V_{qr}\frac{\partial V_{q\theta}}{\partial r}+V_{qz}\frac{\partial V_{q\theta}}{\partial z}+\frac{V_{qr}V_{q\theta}}{r}=\upsilon_q\left(\nabla^2 V_{q\theta}-\frac{V_{q\theta}}{r^2}\right) \tag{2}$$

$$\frac{\partial V_{qr}}{\partial t}+V_{qr}\frac{\partial V_{qr}}{\partial r}+V_{qz}\frac{\partial V_{qr}}{\partial z}-\frac{V_{q\theta}{}^2}{r}=-\frac{1}{\rho_q}\frac{\partial p_q}{\partial r}+\upsilon_q\left(\nabla^2 V_{qr}-\frac{V_{qr}}{r^2}\right) \tag{3}$$

$$\frac{\partial V_{qz}}{\partial t}+V_{qr}\frac{\partial V_{qz}}{\partial r}+V_{qz}\frac{\partial V_{qr}}{\partial z}=g-\frac{1}{\rho_q}\frac{\partial p_q}{\partial z}+\upsilon_q\nabla^2 V_{qz} \tag{4}$$

$$\rho=\sum\alpha_q\rho_q \tag{5}$$

$$\upsilon=\sum\alpha_q\upsilon_q \tag{6}$$

where $\rho_q$ and $\nu_q$ are the density and viscosity of the $q$th phase, respectively and $\alpha_q$ is the volume fraction of the $q$th phase.

In the process of the generation and development of vortex motion, in addition to the spatial distribution of speed, depressions also developed on the surface. Considering the state of the oil spilled on the surface, the air–oil–water three-phase layered distribution was present in the surrounding environment. Because there was almost no interpenetration between the phases, clear interfaces between the phases were observed. The VOF model is the most suitable (Hirt and Nichols, 1981). This model assumes the volume fraction of each phase. In each calculation unit, the sum of the volume fractions is 1, that is,

$$\alpha_a + \alpha_o + \alpha_w = 1 \tag{7}$$

where $\alpha_a$, $\alpha_o$, and $\alpha_w$ represent the volume fractions of the air, oil, and water, respectively.

The method tracks the interface between phases and only necessitates solving the continuity equation of the volume fraction of multiple phases, which greatly simplifies the calculation.

### 3.2. Vortex model

The earliest description of vortex motion was formulated by Rankine (1858). Rankine described a 2D vortex model on a horizontal section and divided the distribution of its tangential velocity into regions. Rankine first proposed the concept of the vortex core radius. In a circumferential area based on a certain radius, the vortex maintains the characteristics of a rigid vortex, while maintaining the same angular velocity. The tangential velocity exhibits a linear relationship with the radial position of the selected fluid micelles. Outside this circle, the vortex is assumed to be a potential vortex extending infinitely. Combining the two distribution curves, the location where they intersect gives the radius of the vortex core. This ideal model indicates that, at the radius of the vortex core, the circulation of the vortex motion reaches its maximum value. Subsequently, the circulation remains fixed as the position expands outwards. From the perspective of circulation, as the radial distance increases, the value of circulation first increases with a power of two, and then remains unchanged after reaching its maximum.

This model first qualitatively describes the velocity distribution during vortex movement and can also roughly predict the velocity of other locations based on the maximum velocity. However, owing to the use of a piecewise function, the speed transition was not smooth, which contradicts the actual observation.

Decades later, Rosenhead (1930) proposed a new model using a unified equation to describe vortex motion. In his model, the circulation no longer reached a maximum at the radius of the vortex core, and it continued to increase radially outwards. Later, Vatistas et al. (1988) improved the model, and the tangential velocity was no longer associated with the maximum circulation value, but rather with the circulation inside the circle at the location. This study compares these types of models. For details, see the following results and discussion. See the appendix for the specific form of the models.

Analyzing the tangential velocity model is helpful for understanding the law of vortex motion. Applying the model to the 3D space and analyzing the distribution and change law of the velocity reveals the mechanism of oil spill movement.

### 3.3. Numerical approach

In this study, a numerical calculation of the free-surface vortex was performed. The relevant numerical calculation method settings and model conditions can be found in Yang et al. (2020). The atmospheric pressure outlet was set on the upper part of the model, and the negative pressure outlet was set at the bottom. The internal impeller of the pump in the experiment rotates at a high speed, and a negative pressure is formed inside, so that the liquid in the oil hood is continuously sucked. The negative pressure outlet position set in the simulation is consistent with the pump position to achieve the same effect. To maintain a stable liquid level, velocity inlets were set on the side of the model to replenish the water in the flow field. The simulation performed a transient-state calculation with a time step of 0.0005 s. The Semi-Implicit-Method for Pressure Linked Equations (SIMPLE) algorithm was used to solve the momentum equation, and the second-order upwind style was used for discretization. When initializing the flow field, it was divided into three layers: gas, oil, and water. To distinguish it from white oil and relate it to the experimental conditions of crude oil after viscosity reduction, the oil density was set to 960 kg/m$^3$ and the viscosity was set to 0.4 Pa s. A constant-coefficient interfacial tension model was added between the phases to simulate the stress state of crude oil in the experiment.

The vortex in the skimmer is complex and exhibits obvious stratification and strong rotation. Therefore, the Renormalization Group (RNG) $k$–$\varepsilon$ model of the Reynolds average equation was used to solve the continuity equation. In complex shear flows with a large strain rate, a vortex, and separation, the RNG $k$–$\varepsilon$ model performs better than the standard $k$–$\varepsilon$ model, which assumes the turbulent viscosity coefficient to be constant. Although some simplifications are made, the RNG $k$–$\varepsilon$ model is still suitable for this study because of its flow computational burden. The law of vortex motion can be studied by comparing and verifying the simulation results and experimental phenomena.

## 4. Results and discussion

### 4.1. Spatial distribution and movement process of crude oil

To describe the movement state of crude oil, an isosurface was established where the oil content inside the flow field was 50% of the simulation results. In Fig. 9, the distribution of the crude oil at the initial moment and the distribution of the tangential velocity on the horizontal sections are shown. At this instant, the velocity at every location in the flow field was 0, and the oil film maintained a horizontal layered state as it floated on the water surface.

Assuming that the bottom surface of the flow field is the surface with $z = 0$ and the upward direction is the positive direction of $z$, four cross-sections with $z = 0.03$ m, $z = 0.1$ m, $z = 0.17$ m, and $z = 0.24$ m were established. These four heights were selected because the liquid surface dented after the vortex was generated. A height of 0.24 m ensured that there was as much of the liquid phase as possible on the cross-section. A minimum height of 0.03 m was used to limit the influence of the bottom boundary layer region on the speed as much as possible.

Fig. 10 compares the movement of crude oil and white oil during the vortex generation process, and also shows the distribution of the tangential velocity at different heights. At 5 s, the oil phase began to accumulate on the free surface, showing an inverted cone shape as shown in Figs. 10 (a-1) and Fig. 10 (b-1). The degree of accumulation of crude oil was higher than that of white oil. A steeper interphase interface appeared between the oil and water. Simultaneously, however, the surface white oil still covered almost the entire surface, and the accumulated oil sunk smaller. At 6 s, the crude oil extended downward to below $z = 0.05$ m, and the white oil was only more concentrated as shown in Figs. 10 (a-2) and Fig. 10 (b-2). At 8 s, both crude oil and white oil flowed to the bottom outlet, formed an oil core on the axis, and flowed continuously downstream. There was almost no crude oil at the

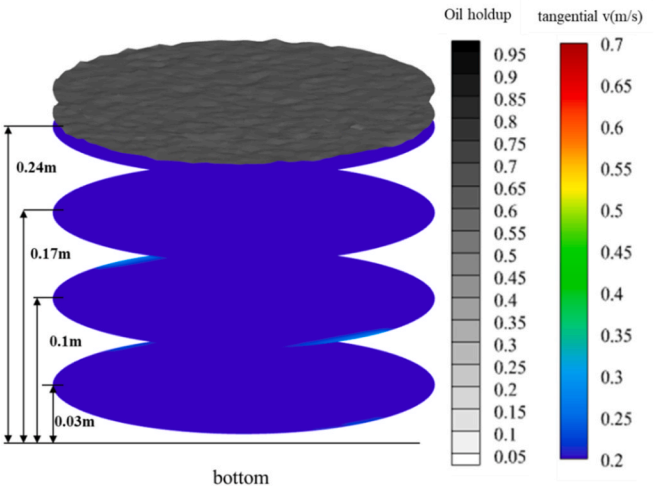


**Fig. 9.** Initial oil film and tangential velocity distribution.

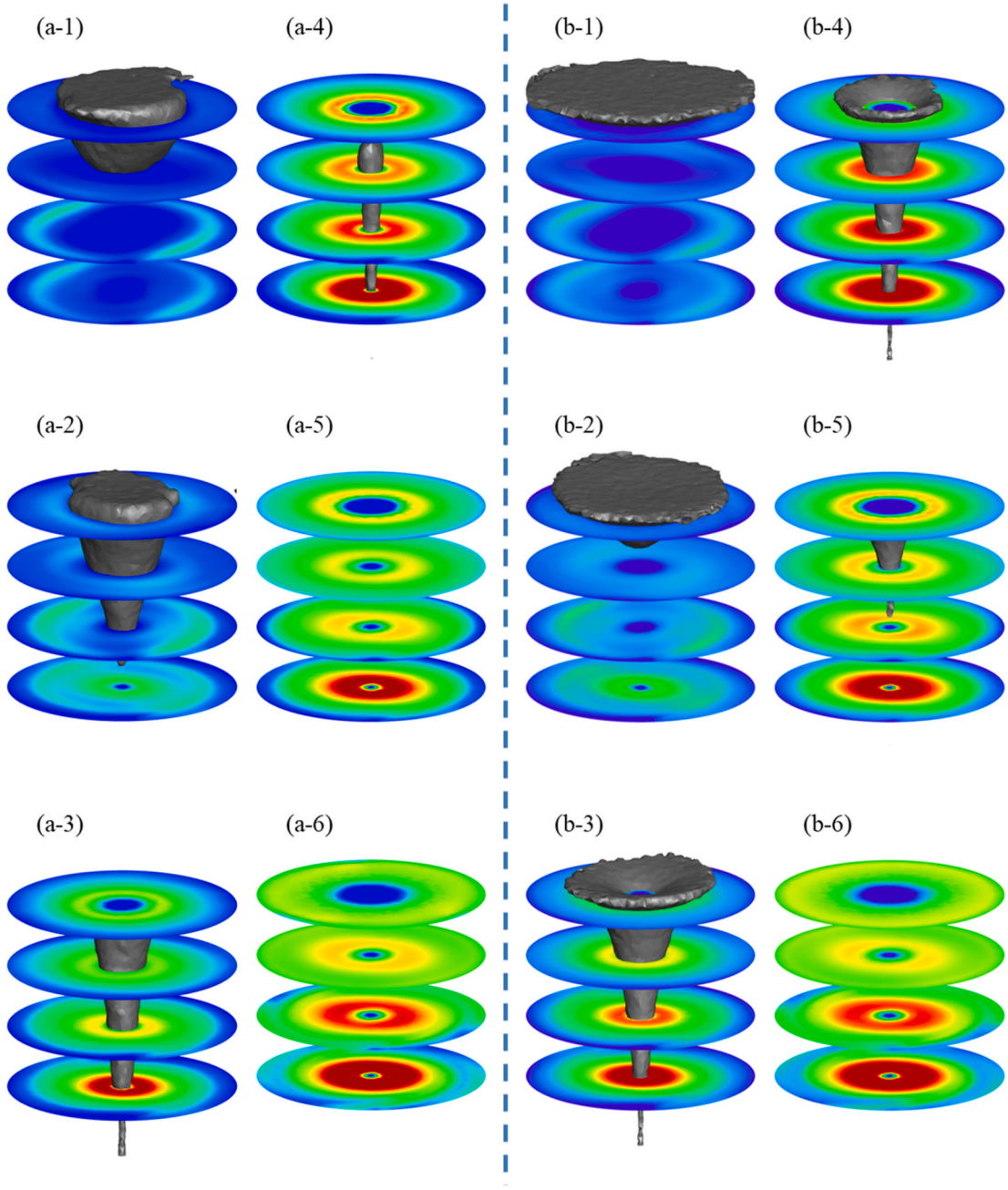


**Fig. 10.** Crude oil phase distribution at (a-1) 5 s, (a-2) 6 s, (a-3) 8 s, (a-4) 9 s, (a-5) 12 s, (a-6) 17.5 s, white oil phase distribution at (b-1) 5 s, (b-2) 6 s, (b-3) 8 s, (b-4) 9 s, (b-5) 12 s, (b-6) 17.5 s and tangential velocity cloud diagram.

liquid level in Figs. 10 (a-3), while the liquid level in Figs. 10 (b-3) still contained a certain amount of white oil. At 9 s, the crude oil had started to flow downstream intermittently as shown in Figs. 10 (a-4). Most of the white oil still existed above the flow field, flowing out continuously with the vortex as shown in Figs. 10 (b-4). Meanwhile, the tangential velocity of the upper layer was at its maximum, after which it began to gradually decrease. The velocity distribution of the white oil flow field was larger than that of the crude oil flow field. At 12 s, almost all the crude oil in the flow field had flowed downstream, and the white oil still had a conical accumulation area above the flow field as shown in Figs. 10 (a-5) and Fig. 10 (b-5). The tangential velocity of the white oil flow field was still greater than that of the crude oil flow field. At 17.5 s, almost both of the two oils had cleaned in both cases as shown in Figs. 10 (a-6) and Fig. 10 (b-6). The tangential velocity at the bottom of the flow field exhibited a certain increasing trend after development, and the upper velocity decreased comparatively. A vortex of a similar scale was observed in the experiment. The liquid surface sagged in the simulation within 10 s of the pump being started in the experiment. The phenomenon was consistent with the simulation results.

### 4.2. *Tangential velocity*

As the vortex developed, the liquid surface became concave, and there may have been a gas phase at the center of the horizontal section. The vortex must be fully developed to reflect its velocity characteristics. Therefore, a liquid level of $z = 0.24$ m at 8 s was selected for further studies on the tangential velocity of the vortex. The tangential velocity-radial position figure of the three models was drawn, and the data obtained by numerical calculation were used as a reference. The radial displacement of the maximum tangential velocity was selected as the

radius of the vortex core. The velocity loop at this location was $\Gamma$, which was introduced into the model for drawing.

As shown in Fig. 11, the velocity distribution trends of the three models were consistent with the simulation results. The tangential velocity of the Rankine model was lower than the simulation result everywhere, and there were significant differences between the results predicted by the Rankine model and the simulation results outside the radius of the vortex core. The tangential velocity of the Rosenhead model was higher than the simulation result everywhere, and the relative deviation was large. The simulation results better fit the Vatistas model. In Fig. 11, there are two areas in which the simulation results show large deviations. Area 1 is located at the center of the vortex, while area 2 is near the sidewall of the skimmer. Owing to the influence of the boundary conditions, the velocities in these two areas were inconsistent with the prediction of the model. The objects of the aforementioned models include potential vortices extending outwards infinitely in a 2D plane. Therefore, the tangential velocity gradually decreases along the radial position, and the changing trend gradually slows. The potential vortex is an ideal phenomenon without friction loss; however, in practice, vortex motion causes energy loss due to friction. Although the energy was replenished through the velocity inlet conditions in the CFD, the tangential velocity in the simulation dropped abruptly near the skimmer wall boundary condition.

To study the distribution law of tangential velocity in a 3D coordinate system, the separation variable method was used to transform the tangential velocity model into a model using the 3D coordinate system. The free-surface vortex is an axisymmetric structure under ideal conditions; therefore, the tangential velocity $V_\theta$ should be a function of the radial position $r$ and height $z$. The expression that introduces separable variables into the tangential velocity is

$$V_\theta = \varphi(r)\cdot\psi(z) \tag{8}$$

As height $z$ was determined, $\psi(z)$ was constant, and the velocity still followed the aforementioned vortex model. By substituting it into the momentum conservation equation in cylindrical coordinates, the linear equation $\psi(z)$ of $z$ can be obtained.

In the flow field, two points were selected, and their tangential velocities at different $z$ values were analyzed. Here, we define dimensionless $r/h$, where $r$ is the radial position and $h$ is the depth of the flow field. As Fig. 12 shows, the $r/h$ value of the selected points is between 0.12 and 0.52, and the interval is 0.04. The selected positions were along the $X$-axis and $Y$-axis directions to analyze the velocity distribution under different $\theta$.

As shown in Fig. 13, the tangential velocity distributions of crude oil and white oil were compared when the oils moved for 7 and 14 s, respectively. It is observed that when $r/h$ is lower than 0.2, the tangential velocity exhibits an obvious nonlinear distribution near the bottom surface. As $z$ decreases, the velocity increases rapidly. There was a very thin boundary layer on the bottom surface, and the velocity had a very large gradient. When $r/h$ ranges from 0.24 to 0.4, the velocity generally changes linearly, as shown in Fig. 13 (c), (d), (g), and (h). However, within this range, the tangential velocity changes slightly with altitude. When $r/h$ is between 0.44 and 0.52, the tangential velocities at different times and positions differ. When the vortex with crude oil on the surface moved to 7 s, the tangential velocity fluctuated slightly with different heights, and the fluctuation on the $Y$-axis was stronger than that on the $X$-axis, as shown in Fig. 13 (a) and Fig. 13 (b). At 14 s, it can be observed from the previous analysis that there was no oil in the region. The velocity at which $z/h$ is larger on the $X$-axis maintains linear characteristics, whereas the velocity in the same area on the $Y$-axis suddenly decreases, which is related to the simulated inlet conditions. As shown in Fig. 13 (b), (d), (f), and (h), the velocity changes suddenly in the $Y$-axis direction because of the influence of the inlet boundary conditions and disturbance of the external flow. In areas less affected by boundary conditions, the tangential velocity is less affected by the height. It is speculated that the tangential velocity distribution still conforms to the law of the theoretical model, but the corresponding velocity circulation parameters change.

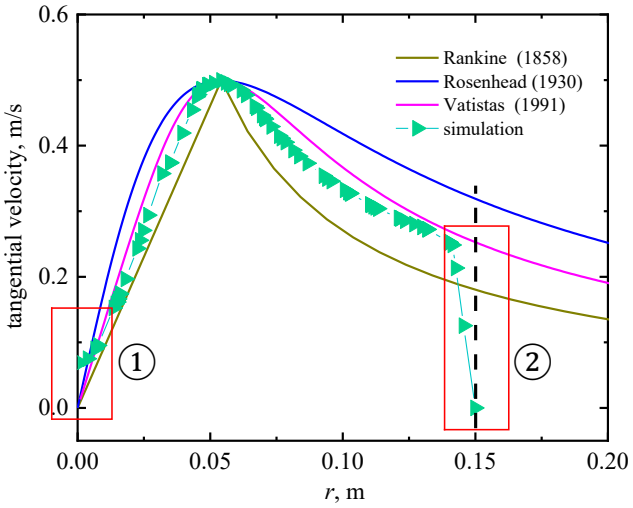


**Fig. 11.** Comparison of tangential velocity of classic models.

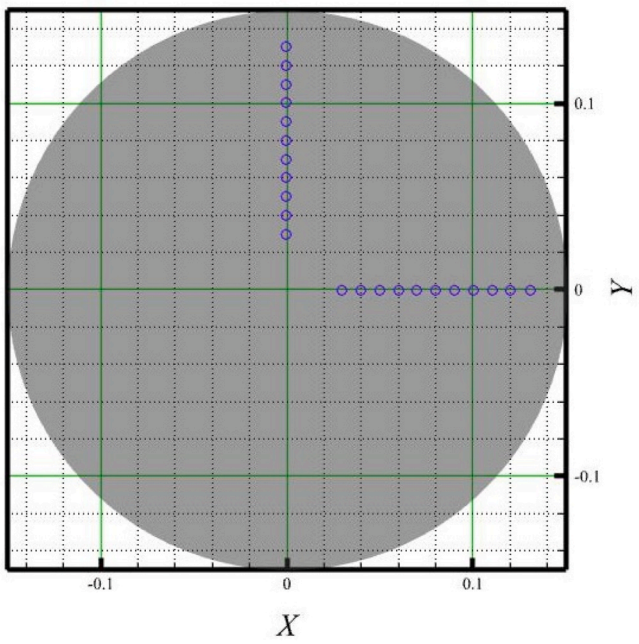


**Fig. 12.** Selection of positions of different $r/h$.

When the surface was covered with white oil, the tangential velocity of the vortex was slightly higher than that of the vortex covered with crude oil at 7 s. The viscosity of the spill oil on the surface and interfacial tension between the phases affects velocity development. When the time reached 14 s, the vortex was fully developed and the velocity difference disappeared, indicating that the final state of the vortex was unrelated to the initial oil spill condition.

### 4.3. Comparison of treatment efficiency

In the simulation, the surface oil slick was initialized and a vortex was created to collect the surface oil phase. Further, the export oil phase flow and treatment efficiency of different oil layer thicknesses and oil product types in the recovery process were compared for the time level.

As shown in Fig. 14, the period from 8.5 s to 11.5 s was intercepted to

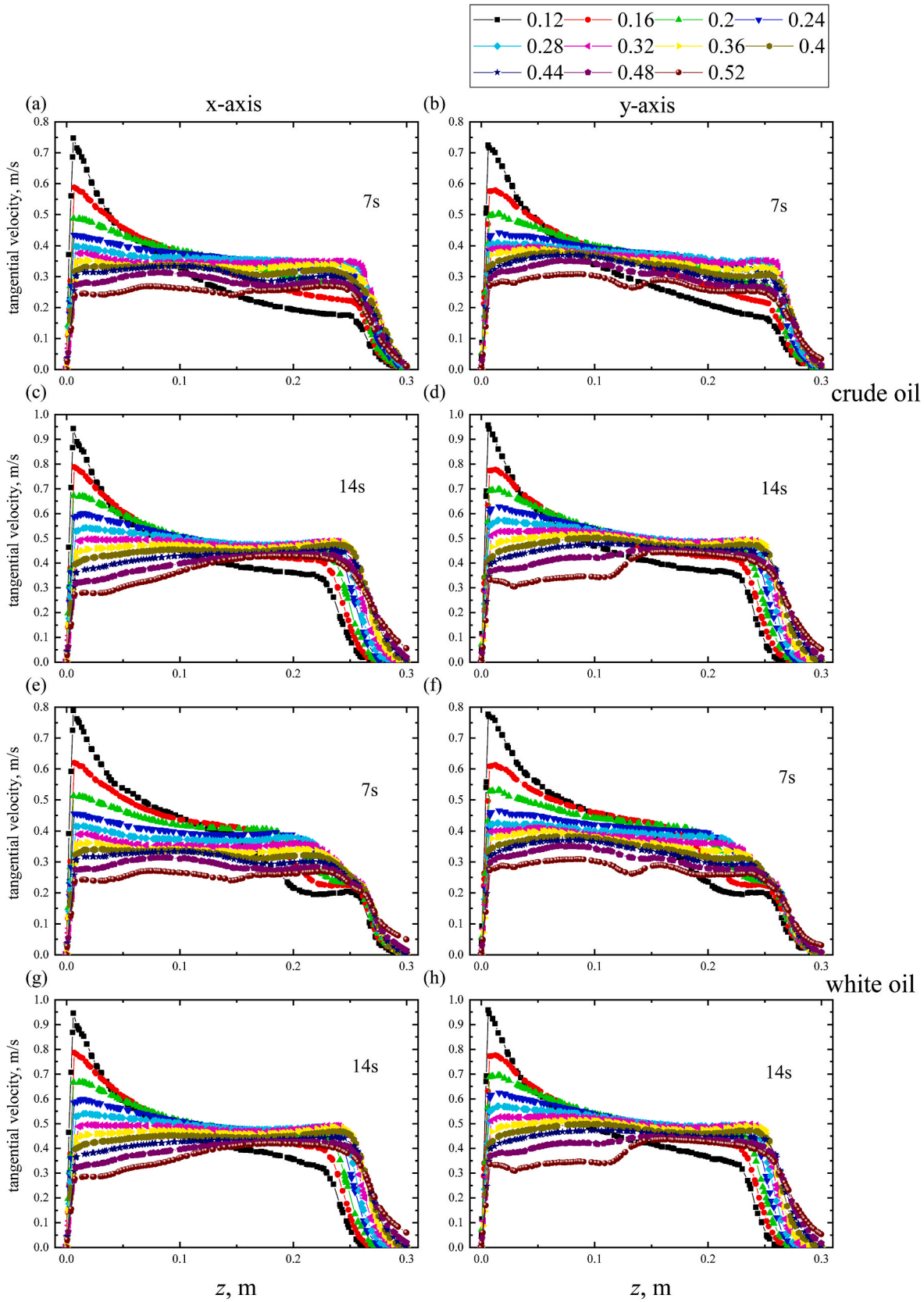


**Fig. 13.** Tangential velocity of $r/h = 0.12$ to 0.52, (a) crude oil at 7 s on the *X*-axis, (b) crude oil at 7 s on the *Y*-axis, (c) crude oil at 14 s on the *X*-axis, (d) crude oil at 14 s on the *Y*-axis, (e) white oil at 7 s on the *X*-axis, (f) white oil at 7 s on the *Y*-axis, (g) white oil at 14 s on the *X*-axis, and (h) white oil at 14 s on the *Y*-axis.

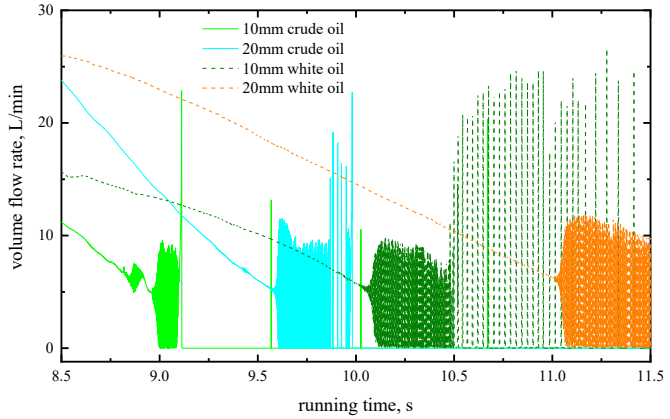


**Fig. 14.** Variation in oil phase flow rate with time under different oil film thicknesses.

compare the outlet oil phase flow when the oil film thicknesses were 10 and 20 mm. During the formation of the vortex, the surface oil was concentrated in the middle. Thereafter, the oil flowed to the outlet as a large mass, so that the oil phase at the bottom outlet had a continuous stage. According to the time curve, crude oil had a steeper curve than white oil, indicating that the oil clumps at the outlet were flatter than those of white oil. In terms of sequence, crude oil was collected earlier than white oil of the same thickness. The density difference between the crude oil and water was smaller than that between the white oil and water. The density, viscosity, and interfacial tension determined the recovery time. Fluidity and diffusion can also affect the recovery process.

Comparing the flow process of different oil products after 11 s, the line in the upper part of Fig. 15 is white oil, and the solid line in the lower part is crude oil. Zooming in on the two circled areas above, many small oil droplets rapidly pass through the bottom outlet. The initial oil film of white oil was 20 mm, and the oil droplets in the second half underwent two types of flow processes. The first one is shown in the enlarged area on the left, where numerous small oil droplets continuously passed through rapidly, and the instantaneous flow reached 10 L/min. The second one is shown in the enlarged area on the right, where the oil droplets are relatively large and the interval between them is also slightly larger, and the instantaneous flow could reach 30 L/min. When the initial oil film of white oil was 10 mm, there were large oil droplets at the outlet after 11 s. The frequency was relatively low, with

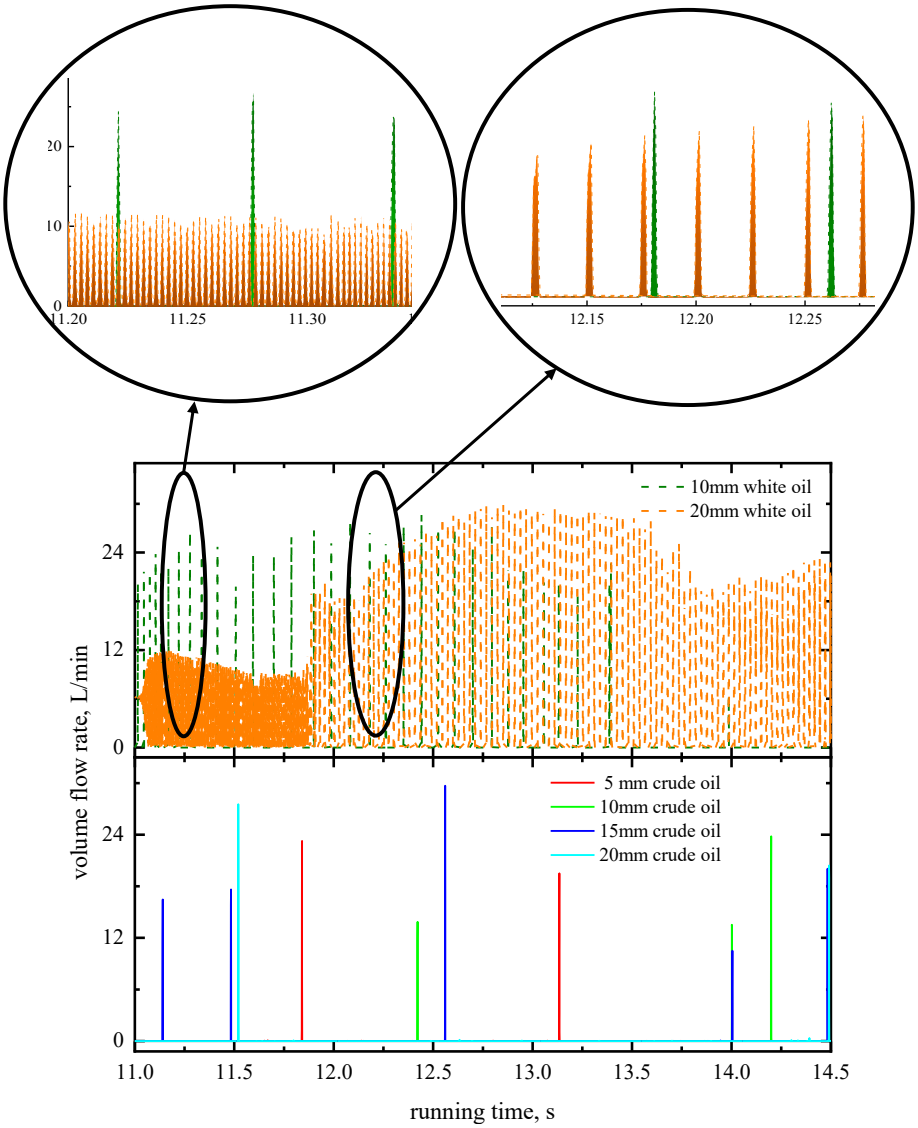


**Fig. 15.** Oil dripping process.

approximately 10 droplets flowing every second. When crude oil was distributed on the surface, there was little oil dripping over the same period, even though the thickness of the oil layer increased from 5 to 20 mm. To compare the sizes of the oil droplets more intuitively, the area enclosed by the curve and $y = 0$ is colored, and the area covered by the color is the volume of the oil droplets. The oil droplet size in the crude oil experiment was within the range that can be observed by the naked eye, which is consistent with the simulation results. The instantaneous oil content at the outlet in the simulation was approximately equal to the experimental results.

The oil phase flow rate through the outlet can be calculated by considering the volume of the oil at the initial moment as the total oil volume. Using the ratio of the flow rate through the outlet and the total volume as the cumulative oil spill treatment efficiency, the law of cumulative treatment efficiency over time can be obtained. As shown in Fig. 16, the recovery start times were different because the types of oil were different. The recovery of crude oil generally occurred earlier than that of white oil. The recovery process of white oil gradually slowed after the dotted line. Once the cumulative treatment efficiency was higher than 80%, the recovery capacity suddenly decreased. In contrast to crude oil, the reduction in the processing rate occurred after the cumulative processing efficiency reached 95% or higher. The processing efficiency values for several key time points are listed in Table 1. The thicker the crude oil, the earlier the recovery process started; the thinner the crude oil, the faster the recovery rate. After the thickness of the white oil increased, the recovery process did not change, but the recovery rate decreased. For both crude oil and white oil, the final cumulative treatment efficiency was above 95%. For the small space enclosed by the skimmer, the oil film was almost completely recovered within 20 s. In the simulation, the skimmer was fixed, and liquid in the same area could be processed repeatedly. The oil remaining on the liquid surface was affected by the continuous action of the vortex, and eventually, most of it was sucked to the bottom of the vortex. Table 1 also shows that a large amount of recycling work was completed in a very short period. For the 5 mm crude oil film, for example, 63% of oil phase was recovered between 7 s and 8 s. Therefore, the simulation results can be referred to in practical engineering applications. In the experiment, the cumulative treatment efficiency cannot reach 100% because of the emulsification. The simulation results were qualitatively analyzed for different oils and thicknesses.

### 4.4. Comparison of separation performance

The internal pressure of the oil spill separation device can reflect energy consumption and provide technical parameters for the further separation of oil–water mixtures. The pressure of the overflow pipe was the value relative to that of the free surface, and the pressure was 0 when the water surface was static. Fig. 17 (a) shows the change in overflow pipe pressure. When the pump frequency was determined, the total inlet flow was changed by adjusting the valve opening, and the pressure decreased as the inlet flow increased. When the frequency of the pump increased, a higher internal pressure appeared at the same inlet flow. This is because reducing the valve opening increased the flow resistance and pressure. When white oil was used for the same experiment, the pressure also decreased with an increase in the flow rate. Given the same starting frequency of the pump, the white oil experiment can often give a much larger inlet flows. In the crude oil experiment, the pump frequency was increased from 20 to 40 Hz, and the flow rate was increased from 8 to 40 L/min. In contrast, in the white oil experiment, the pump frequency increased from 25 to 30 Hz, and the flow rate increased from 15 to 85 L/min. The data indicate that the flow resistance of crude oil is greater than that of white oil, and the rheology measurement also illustrates this point. Moreover, for the same flow, crude oil exhibits a higher viscosity and coefficient of friction. And for the same distance, it experiences a greater pressure loss than white oil. Conversely, crude oil aggregates more easily than white oil, and when aggregated oil interacts with the wall surface, it hinders movement, increasing flow resistance.

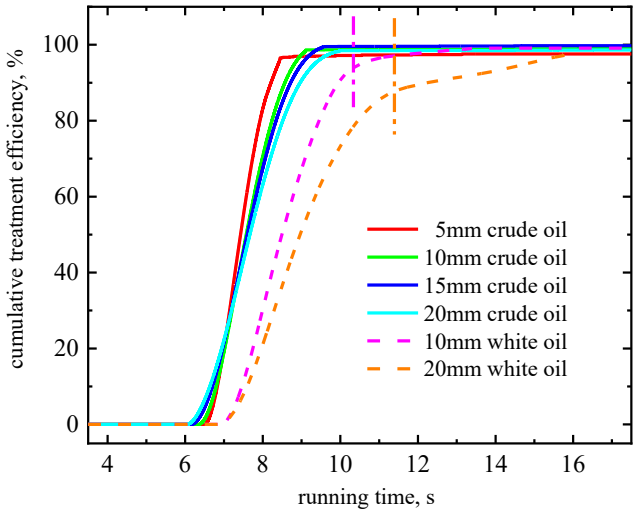


**Fig. 16.** Cumulative treatment efficiency of the two oils.

**Table 1**
Cumulative treatment efficiency of different amounts of oil, %.

| Oil film thickness | Recovery time | | | | | |
|---|---|---|---|---|---|---|
| | 6.5s | 7s | 8s | 10s | 15s | 18s |
| 5 mm | 0 | 20.098 | 83.131 | 97.190 | 97.565 | 97.571 |
| 10 mm | 1.392 | 19.028 | 70.617 | 98.683 | 98.941 | 99.040 |
| 15 mm | 4.343 | 21.510 | 67.440 | 99.539 | 99.745 | 99.755 |
| 20 mm | 6.457 | 22.242 | 63.090 | 98.456 | 98.558 | 98.600 |
| 10 mm | 0 | 0.295 | 30.263 | 90.716 | 99.103 | 99.106 |
| 20 mm | 0 | 0.359 | 21.055 | 73.266 | 95.486 | 97.622 |

The relationship between the flow rate and pressure in the overflow pipe is shown in Fig. 17 (b). As the flow rate of the overflow pipe increased, the pressure increased linearly. Different pump frequencies roughly determined the range of flow, but did not affect the relationship between the pressure and flow rate. The maximum flow rate at the overflow port was approximately 22 L/min.

The overflow and underflow ports were sampled and the samples were placed in a graduated cylinder and allowed to stand until the mixture formed layers. The volume and total volume of the oil were determined, and the ratio of the volume was the oil content of the sample. The sampling results indicated that the oil content of the overflow port was always higher than that of the underflow port. As shown in Fig. 18, this was one of the sampling results. The left side shows the overflow port liquid sample, and the right side shows the underflow port sample. The ratio of the oil content of the overflow to the underflow is between 1.5 and 8.4, and in most cases is between 2.5 and 5.

The ratio of the overflow flow rate to the total inlet flow rate is defined as the split ratio, and the ratio of the overflow and inlet oil flow rates is defined as the recovery efficiency. Eq. (9) is used to calculate the recovery efficiency, where $Q_{over}$ refers to the oil volume flow rate of the overflow, and $Q_{in}$ refers to the oil volume flow rate of the inlet.

$$\varepsilon = \frac{Q_{over}}{Q_{in}} \times 100\% \tag{9}$$

As Fig. 19 shows, the relationship between the recovery efficiency and the split ratio is linear. An et al. (2021) noted that the relationship between the recovery efficiency and split ratio is unrelated to the amount of oil spilled; therefore, the recovery efficiency of crude oil is more sensitive to changes in the split ratio. As the split ratio increases, the recovery efficiency also increases. The split ratio was calculated

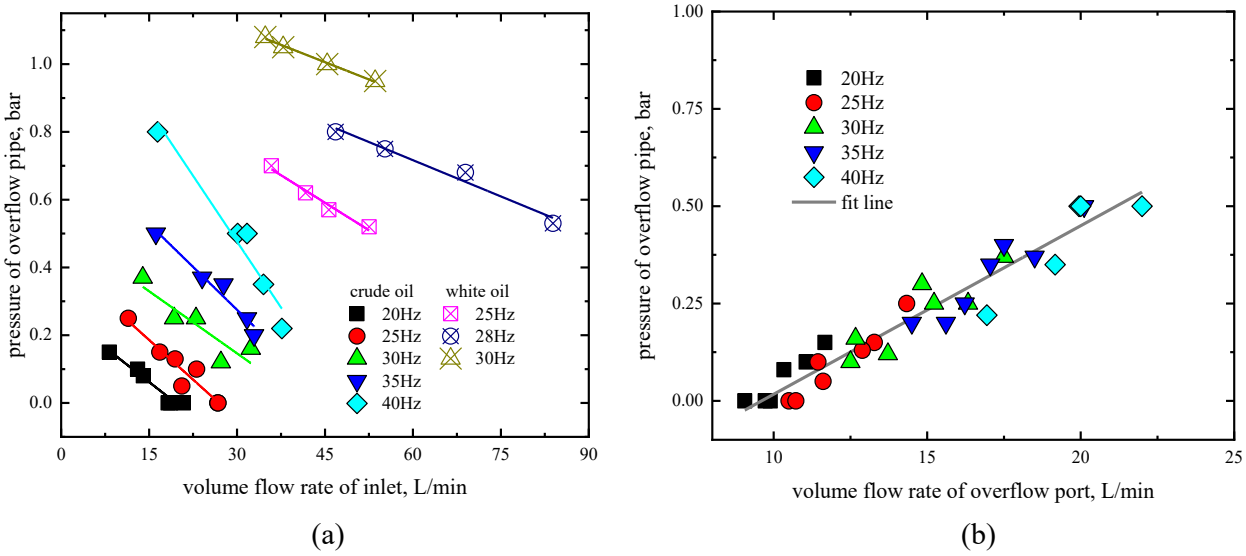


**Fig. 17.** Relationship between pressure and flow rate of (a) inlet and (b) overflow.

**Fig. 18.** One of the sampling results at overflow port and underflow port.

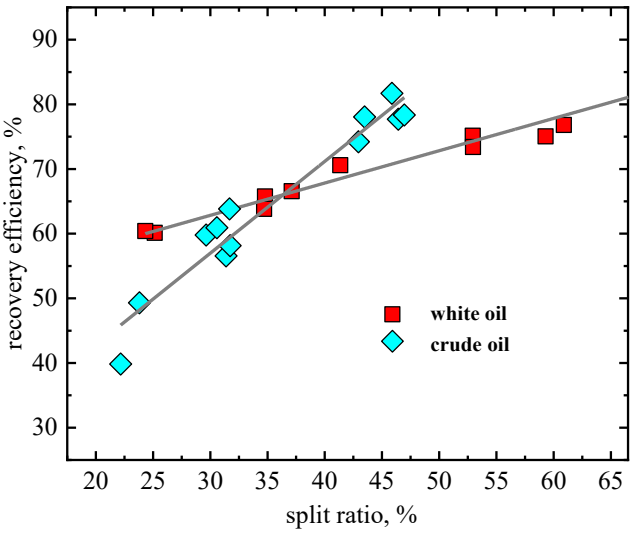


**Fig. 19.** Recovery efficiencies in different oil experiment.

according to Eq. (9), assuming the same inlet and outlet oil-phase flow rates. When the split ratio reaches 100%, the recovery ratio should be 100%. However, the relationship between the split ratio and recovery efficiency of crude oil did not match the prediction. This difference can be attributed to two reasons. First, for crude oil, the linear relationship is applicable only to lower split ratios. Second, the slip velocity of crude oil is different, which also leads to different oil contents of the fluid involved in cyclone separation under different split ratios. These factors limit the linear law of recovery efficiency.

## 5. Conclusions and suggestions

Experimental tests and CFD simulations were performed to investigate the working characteristics of an oil spill treatment device composed of a free-surface vortex oil skimmer and an axial hydrocyclone separator. A small-scale recovery and separation device was fabricated and tested, and a model of the same scale was established via simulation. The flow, pressure, and content data for each phase were collected during the experiment. The experiment verified that the VOF model and RNG $k$–$\varepsilon$ model can be used to calculate vortex motion and can simulate similar flow states with a flow computational burden.

The spatial distribution of the tangential velocity was derived by combining a 2D velocity model with the governing equation of the cylindrical coordinate system. According to this equation, the tangential velocity is linearly distributed in the vertical direction, and the trend of the change must be judged according to the boundary conditions or the interphase interface. Further studies may explain the nature of the vortex-recovered surface oil. Because of the different properties of oil, the state of movement in the vortex is significantly different. After aggregation, different forms of oil exhibit different oil properties. The free-surface vortex can also recover oil with a high density and viscosity, and the oil is more likely to move in the form of large oil droplets.

The experiment verified the separation characteristics of axial hydrocyclone in crude oil processing. The differences in the influence of oil properties on the separation law were compared. The flow in the separation equipment is influenced by the rheological properties of the mixture. The spin state and energy loss were closely related to the treatment fluid. Within this range, increasing the split ratio can improve the separation efficiency. The law exhibits a similar performance for different oils.

The flow within the recovery and separation devices is extremely complex. The results of this study can inform the optimal design of equipment in the treatment of liquid mixtures with density differences in related fields, such as the sewage treatment and petroleum industry.

## CRediT authorship contribution statement

**Meng Yang:** Writing – original draft, Validation, Writing – review & editing. **Lin-tong Hou:** Data curation, Investigation. **Li-song Wang:** Visualization, Resources. **Shuo Liu:** Conceptualization, Funding acquisition. **Jing-yu Xu:** Project administration, Funding acquisition.

## Declaration of competing interest

The authors declare that they have no known competing financial interests or personal relationships that could have appeared to influence the work reported in this paper.

## Data availability

Data will be made available on request.

## Acknowledgements

This work present here is financially supported by National Natural Science Foundation of China (no. 12102436) and the Strategic Priority Research Program of the Chinese Academy of Science (Grant no: XDB22030101).

## Appendix

The vortex model proposed by Rankine (1858) is divided into two regions, and the boundary between these regions is a circle formed by the radius of the vortex core. The inner area of the boundary is a rigid vortex and the outer portion is a potential vortex. The velocities at the boundary line are equal. The Rankine vortex model is expressed as follows:

$$V_\theta = \frac{\Gamma r}{2\pi r_m^2}, r \le r_m$$
$$V_\theta = \frac{\Gamma}{2\pi r}, r \ge r_m \tag{A.1}$$

In Eq. (A.1), $r$ is the radial position and $r_m$ is the radius of the vortex core.

Rosenhead (1930) proposed the following empirical formula based on experimental data and mathematical analysis:

$$V_\theta = \frac{\Gamma}{2\pi}\frac{r}{r^2 + r_m^2} \tag{A.2}$$

Vatistas et al. (1988) proposed an empirical formula for tangential velocity based on the amount of circulation:

$$V_\theta = \frac{\Gamma}{2\pi}\frac{r}{\sqrt{r^4 + r_m^4}} \tag{A.3}$$

Eq. (8) can be substituted into Eq. (4) according to the separation of variables method. If $\varphi(r)$ is expressed in the form of Eq. (A.2), we obtain:

$$V_r = -\frac{4r\upsilon}{r^2 + r_m^2} + \frac{\left(r^2 + r_m^2\right)r\upsilon}{2r_m^2\psi(z)}\psi''(z) + \frac{\left(r^2 + r_m^2\right)rV_z}{2r_m^2\psi(z)}\psi'(z) \tag{A.4}$$

According to actual observations, at an infinite distance of the flow field, the radial and axial velocities of the vortex both tend toward 0, so $\psi''(z) = 0$ and $\psi'(z)$ is a constant. When $z = h$, the flow was on the free surface; $\psi(z) = 1$. In summary, we obtain:

$$\psi(z) = k(z - h) + 1 \tag{A.5}$$

The tangential velocity of the 3D flow field can be expressed as:

$$V_\theta = \frac{\Gamma}{2\pi}\frac{r}{r^2 + r_m^2}[k(z - h) - 1] \tag{A.6}$$

## References

Abhinav, D., Pradipta, C., 2021. A review on physical remediation techniques for treatment of marine oil spills. J. Environ. Manag. 288, 112428.
Alves, T.M., Kokinou, E., Zodiatis, G., 2014. A three-step model to assess shoreline and offshore susceptibility to oil spills: the South Aegean (Crete) as an analogue for confined marine basins. Mar. Pollut. Bull. 86 (1), 443–457.
Alves, T.M., Kolinou, E., Zodiatis, G., Lardner, R., Panagiotakis, C., Radhakrishnan, H., 2015. Modelling of oil spills in confined maritime basins: the case for early response in the Eastern Mediterranean sea. Environ. Pollut. 206 (206), 390–399.
An, W., Zhang, Q., Zhao, J., Qu, L., Liu, S., Yang, M., Xu, J., 2021. Mechanism investigation on a novel oil recovery skimmer coupling free surface vortex and cyclone separation. ACS Omega 6, 20483–20491.
Bayat, Z., Hassanshahian, M., Hesni, M.A., 2015. Enrichment and isolation of crude oil degrading bacteria from some mussels collected from the Persian Gulf. Mar. Pollut. Bull. 101 (1), 85–91.
Burgers, J.M., 1948. A mathematical model illustrating the theory of turbulence. Adv. Appl. Mech. 1, 171–199.
Cao, R., Chen, H., Rong, Z., Lv, X., 2021. Impact of ocean waves on transport of underwater spilled oil in the Bohai Sea. Mar. Pollut. Bull. 171, 112702.
Chan, S.N., Guo, J., Lee, J.H.W., 2022. Physical and numerical modeling of swirling flow in a scroll vortex intake. J. Hydro-environ. Res. 40, 64–76.
Einstein, H.A., Li, H., 1955. Steady vortex flow in a real fluid. La Houille Blanche 4, 483–496.
Eronat, A.H., Bengil, F., Neser, G., 2019. Shipping and ship recycling related oil pollution detection in Çandarlı Bay (Turkey) using satellite monitoring. Ocean. Eng. 187, 106157.
Etkin, D.S., Nedwed, T.J., 2021. Effectiveness of mechanical recovery for large offshore oil spills. Mar. Pollut. Bull. 163, 111848.
Fingas, M., 2011. Oil spill science and technology prevention, response, and cleanup. In: Oil Spill Science and Technology. Elsveir Science LTD, Burlington.
Giron-Sierra, J.M., Gheorghita, A.T., Angulo, G., Jimenez, J.F., 2015. Preparing the automatic spill recovery by two unmanned boats towing a boom: development with scale experiments. Ocean. Eng. 95, 23–33.
Hirt, C.W., Nichols, B.D., 1981. Volume of Fluid (VOF) method for the dynamics of free boundaries. J. Comput. Phys. 39, 201–225.

Hsiao, T., Chen, D., Li, L., Greenberg, P., 2010. Development of a multi-stage axial flow cyclone. Aerosol Sci. Technol. 44, 253–261.
Kandanelli, R., Meesala, L., Kumar, J., Raju, C.S.K., Peddy, V.C.R., Gandham, S., Kumar, P., 2018. Cost effective and practically viable oil spillage mitigation: comprehensive study with biochar. Mar. Pollut. Bull. 128, 32–40.
Kataoka, H., Tomiyama, A., Hosokawa, S., Sou, A., Chaki, M., 2008. Two-phase swirling flow in a gas-liquid separator. J. Power Energy Syst. 2, 1120–1131.
Kataoka, H., Shinkai, Y., Tomiyama, A., 2009. Pressure drop in two-phase swirling flow in a steam separator. J. Power Energy Syst. 3, 382–392.
Khazam, O., Krestra, S.M., 2008. Mechanisms of solids drawdown in stirred tanks. Can. J. Chem. Eng. 86, 622–634.
Kumar, R.A., Nair, R.R., Prabhu, M., Srikrishnan, A.R., 2017. Vortex formation during draining from cylindrical tanks: effect of drain port eccentricity. J. Aero. Eng. 30 (5).
Liow, J., Oakman, O.A., 2018. Performance of mini-axial hydrocyclones. Miner. Eng. 122, 67–78.
Liu, L., Bai, B., 2016. Scaling laws for gas-liquid flow in swirl vane separators. Nucl. Eng. Des. 298, 229–239.
Liu, S., Zhang, J., Wang, L., Xu, J., 2020. Separation mechanism and influential factor study on vane-type-associated petroleum gas separator. Separ. Purif. Technol. 250, 117274.
Liu, X., Wirtz, K.W., 2009. The economy of oil spills: direct and indirect costs as a function of spill size. J. Hazard Mater. 171, 472–477.
Matsubayashi, T., Katono, K., Hayashi, K., Tomiyama, A., 2012. Effects of swirler shape on swirling annular flow in a gas-liquid separator. Nucl. Eng. Des. 249, 63–70.
Mih, W.C., 1990. Discussion of "Analysis of fine particle concentrations in a combined vortex". J. Hydraul. Res. 28, 392–395.
Mulligan, S., Casserly, J., Sherlock, R., 2016. Effects of Geometry on strong free-surface vortices in subcritical approach flows. J. Hydraul. Eng. 142, 04016051.
Mulligan, S., Creedon, L., Casserly, J., Sherlock, R., 2019. An improved model for the tangential velocity distribution in strong free-surface vortices: an experimental and theoretical study. J. Hydraul. Res. 57 (4), 547–560.
Ornitz, B.E., Champ, M.A., 2002. Oil spills first principles. Prevention and best response. Oil Spills First Principlest Elsevier Science, pp. 302–308. https://doi.org/10.1016/B978-008042814-7/50025-2.
Rankine, W.J.M., 1858. A Manual of Applied Mechanics. Ed. 1. Charles Griffin, London.
Rosenhead, L., 1930. The spread of vorticity in the wake behind a cylinder. In: Proceedings of the Royal Society A. Series A, Containing Papers of a Mathematical and Physical Character, 127, pp. 590–612.
Shemshi, R., Kabiri-Samani, A., 2016. Swirling flow at vertical shaft spillways with circular piano-key inlets. J. Hydraul. Res. 55 (2), 248–258.
Shi, S., Xu, J., Sun, H., Zhang, J., Li, D., Wu, Y., 2012. Experimental study of a vane-type pipe separator for oil-water separation. Chem. Eng. Res. Des. 90, 1652–1659.
Tastan, K., Yildirim, N., 2018. Effects of intake geometry on the occurrence of a free-surface vortex. J. Hydraul. Eng. 144 (4).
Tkalich, P., 2000. Numerical simulations of oil spills and oil combating techniques. In: Proceedings, Conference on Oil and Hydrocarbon Spills II: Modelling, Analysis and Control. Las Palmas, Spain, September 20-22, pp. 51–59.
Tsai, C.J., Chen, D.R., Chein, H.M., Chen, S.C., Roth, J.L., Hsu, Y.D., Li, W.L., Biswas, P., 2004. Theoretical and experimental study of an axial flow cyclone for fine particle removal in vacuum conditions. J. Aerosol Sci. 35, 1105–1118.
Vatistas, G.H., Lin, S., Li, P.M., 1988. A similar profile for the tangential velocity in vortex chambers. Exp. Fluid 6, 135–137.
Ventikos, N.P., Vergetis, E., Psaraftis, H.N., Triantafyllou, G., 2004. A high-level synthesis of oil spill response equipment and countermeasures. J. Hazard Mater. 107, 51–58.
Wang, G., Yan, C., Fan, G., Wang, J., Xu, J., Zeng, X., Liu, A., 2019. Experimental study on a swirl-vane separator for gas-liquid separation. Chem. Eng. Res. Des. 151, 108–119.
Wei, L., Hu, Z., Dong, L., Zhao, W., 2015. A damage assessment model of oil spill accident combining historical data and satellite remote sensing information: a case study in Penglai 19-3 oil spill accident of China. Mar. Pollut. Bull. 91 (1), 258–271.
Xu, W., Tan, Y., Li, M., Sun, J., Xie, D., Liu, Z., 2020. Effects of surface vortex on the drawdown and dispersion of floating particles in stirred tanks. Particuology 49, 159–168.
Yang, M., Liu, S., Xu, W., Xu, J., 2020. Numerical and experimental studies of an oil slick recovery method that uses a free surface vortex. ACS Omega 5, 31332–31341.
Yu, F., Fan, Z., Hu, H., Zhao, Y., Tang, J., Chen, G., 2020. A regional parameterization method for oil spill susceptibility assessment in Beibu Gulf. Ocean. Eng. 215, 107776.
Zhang, C., Han, L., Shi, X., 2016. Modified assessment methodology for mechanical recovery capacity for oil spill response at sea. Aquatic Procedia 3, 29–34.